Laser-Reduced $BiVO_4$ for Enhanced Photoelectrochemical Water Splitting

Mariam Barawi,[a] Miguel Gomez-Mendoza,[a] Freddy E. Oropeza,[a] Giulio Gorni,[b] Ignacio J Villar-Garcia,[c] Sixto Giménez,[d] Victor A. de la Peña O'Shea [a] and Miguel García-Tecedor [a*]*

[a]*Photoactivated Processes Unit, IMDEA Energy, Avda. Ramón de la Sagra, 3, Móstoles, 28935, Spain.*

[b]*CLÆSS Beamline, ALBA Synchrotron, Carrer de la Llum 2-26, Cerdanyola del Valles, 08290, Spain.*

[c]*NAPP Endstation, CIRCE Beamline, ALBA Synchrotron, Carrer de la Llum 2-26, Cerdanyola del Valles, 08290, Spain.*

[d]*Institute of Advanced Materials (INAM), Universitat Jaume I, Avda. Vicente Sos Baynat, s/n, Castelló, 12006, Spain.*

Email: victor.delapenya@imdea.org , miguel.tecedor@imdea.org

KEYWORDS. *Photoelectrochemistry, $BiVO_4$, Solar Fuels, Surface Chemistry, Electrochemical Impedance Spectroscopy, Transient Absorption Spectroscopy.*

Abstract

The present study proposes a laser irradiation method to superficially reduce $BiVO_4$ photoelectrodes that boosts their water oxidation reaction performance. The origin of this enhanced performance towards Oxygen Evolution Reaction (OER) was studied by a combination of a suite of structural, chemical, and mechanistic advanced characterization techniques including XPS, XAS, EIS and TAS, among others. We found that the reduction of the material is localized at the surface of the sample and that this effect creates an effective n-type doping and a shift to more favorable energy band positions towards water oxidation. This thermodynamic effect, together with the change in sample morphology to larger and denser domains, result in an extended lifetime of the photogenerated carriers and an improved charge extraction. In addition, the stability in water of the reduced sample was also confirmed. All these effects, result on a two-fold increase in the photocurrent density of the laser treated samples.

Introduction

$BiVO_4$ is one of the most attractive candidates for photoelectrochemical (PEC) water splitting due to its suitable optoelectronic properties as its bandgap (2.4 eV) and its energy band edge positions.[1,2] However, it also suffers from poor carrier transport and surface recombination.[3,4,5] In order to overcome these limitations, a great effort has been made to enhance the performance of $BiVO_4$ photoanodes through different approaches such as nanostructuring,[6] heterostructuring with other metal oxides,[7] the deposition of co-catalysts[8] and the employment of post-synthetic treatments.[9]

Among the different reported post-synthetic treatments, several studies were focused on different light exposures enhancing the performance of $BiVO_4$. An improvement in the photocurrent onset was reported on $BiVO_4$ photoanodes after long UV exposure due to a decrease in the number of defect states at the surface, mainly dangling oxygen centers.[10] Photocharging effect after illumination of $BiVO_4$ photoanodes at open circuit conditions (OCP), was also reported, finding that this beneficial effect was the result of the formation of a capacitive layer which reduces surface recombination.[8] Very recently, Mas-Marzá *et al*. have shown that the segregation of Bi species to the surface, with the concomitant formation of intrabandgap states associated to oxygen vacancies after light-aging treatments, lead to an enhanced photocurrent in $BiVO_4$ photoanodes for the oxidation of benzyl alcohol.[11] After the majority of light-exposure treatments in $BiVO_4$ photoanodes, the generation of oxygen vacancies was detected. Interestingly, and following the highly-reported black-TiO_2[12,13,14] there is an ongoing debate about the role of these defects in the final performance of metal oxide photoelectrodes.[15,16,17] On this direction, several works reported oxygen-vacancies-rich $BiVO_4$ photoanodes based on different post-synthetic methods. The hydrogeneration of $BiVO_4$ films were reported to generate oxygen vacancies and hydrogen impurities increasing the donor density.[18] Wang and co-workers reported a consecutive-calcination method to enhance the performance of $BiVO_4$ photoanodes by the generation of oxygen vacancies which act as shallow donors.[19] A sulfur oxidation strategy was also reported by this group to *in situ* form oxygen vacancies in $BiVO_4$, boosting the charge separation efficiency over 98%.[20] Black-$BiVO_4$ was reported by reducing $BiVO_4$ under hydrogen plasma treatment, leading to a bandgap reduction of approx. 0.3 eV and improved transport and charge separation.[21] However, recent studies in $BiVO_4$ demonstrate that bulk oxygen vacancies act as deep hole traps unable to participate in water oxidation, while surface oxygen vacancies boosted

water oxidation on $BiVO_4$ due to the creation of surface states close to the conduction band which accelerate charge transport and charge extraction.[22,23,24] Additionally, surface oxygen vacancies were also recently reported to enhance surface reactivity in $BiVO_4$ photoanodes.[25]

Time-resolved spectroscopies, as Transient Absorption spectroscopy and Electrochemical Impedance spectroscopy (EIS), have emerged as powerful tools for the analysis of the different physical processes, as charge generation, extraction and recombination, taking place in semiconducting photoelectrodes at different time scales.[26,27,28,29,30,31]

With these premises, a laser pulse was employed in the present study to selectively reduce the surface of $BiVO_4$, leading to an enhanced photoelectrocatalytic behavior towards the Oxygen Evolution Reaction (OER). The reduced material was analyzed through a wide range of advanced materials characterization techniques, through a deep structural and physico-chemical study of surface and volume. Additionally, a combination of EIS and TAS was employed to study the charge dynamics to unveil the origin of the enhanced behavior towards water oxidation.

Results and discussion

To fabricate the reduced Zr doped $BiVO_4$, the electrodeposited pristine samples on FTO (fluorine doped tin oxide, F: SnO_2) substrates, described in supporting Information, were irradiated with different 355 nm laser pulse energies (1, 10, 20 and 30 mJ) during 30 s of exposure (**Figure 1a**). On the other hand, **Figure 1b** shows the photocurrent density at 1.8 V vs RHE as a function of the laser output energy. The plot exhibits a volcano-shape profile with a maximum at 10 mJ output energy (see also cyclic voltammetries, CV, Figure S1, Supporting Information).

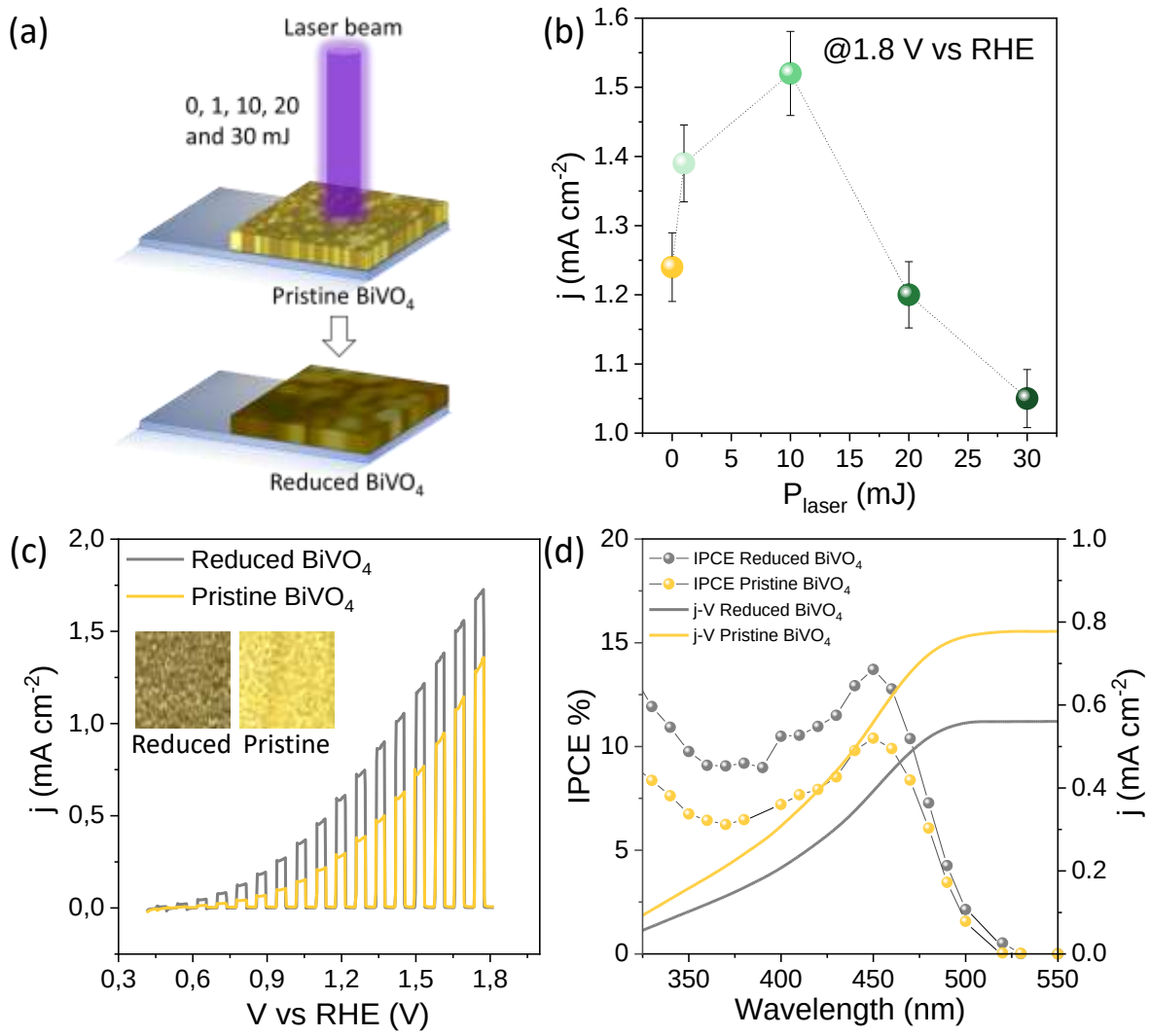

Figure 1. (a) Scheme of the laser-based reduction process on $BiVO_4$ photoanodes. (b) Volcano plot showing the measured photocurrent at 1.8 V vs RHE versus laser energies in 0.1 M potassium phosphate (KPi) buffer solution of pH 7.5 as electrolyte. (c) Linear sweep voltammetry (LSV) under 1 Sun (100 mW cm^{-2}) chopped illumination on the analyzed samples. (d) IPCE spectra acquired at 1.23 V vs RHE and the correspondent estimated photocurrent densities.

As it will analyzed in depth along this study, the laser irradiation induces a reduction at the surface of the pristine $BiVO_4$ with its concomitant creation of oxygen vacancies. This process leads to an enhanced photoelectrocatalytic behavior which improves up to 10 mJ. However, an

additional increase in the laser energy leads to a sample degradation doe to material loss, decreasing the PEC performance. Therefore, from now on, this study will be focused on the comparison between pristine and reduced $BiVO_4$ with the optimized laser treatment conditions (10 mJ for 30s). **Figure 1c** shows the j-V response of the two analyzed samples, where the reduced sample exhibits a two-fold increase in the photocurrent density in comparison with the pristine sample (from 0.29 mA cm^{-2} in the pristine sample to 0.6 mA cm^{-2} in the reduce one, at 1.23 V vs RHE). Both analyzed photoelectrodes show a higher photocurrent when back-illuminated, Figure S2 Supporting Information, due to the lower diffusion length of the photogenerated electrons which have to hop between VO_4 tetrahedra, as it has been reported for $BiVO_4$.[32] Figure S3a shows the linear sweep voltammograms (LSV) of the analysed samples under aqueous electrolyte and under the presence of a hole scavenger (Na_2SO_3). At large anodic bias (V > 1.4 V vs RHE), the reduced $BiVO_4$ shows around 10% higher catalytic efficiency than the pristine $BiVO_4$, while the calculated charge separation efficiency was higher in the reduced sample along the whole potential window, demonstrating the validity of this post-synthetic treatment for enhancing the PEC performance of $BiVO_4$. In addition, the stability of the laser-reduced and the pristine $BiVO_4$ was proved along 4 hours of operation, as shown in Figure S4. As it can be observed, the photocurrent of the reduced sample decreased faster (in two hours it suffers from a 50% loss) than the pristine one, even it shows a stable behavior over the first hour of operation. Furthermore, after 3 hours, the photocurrent of the reduced sample achieves the value of the pristine one, indicating the reoxidation of the laser-reduced sample under this operation conditions (anodic potential and aqueous media). Besides, Figure S5 shows the theoretical and experimental oxygen generation as well as the calculated Faradaic Efficiency (FE). FE values close to 100% were obtained on the

laser-reduced $BiVO_4$ photoanode, proving the ability of this material to generate oxygen. The scattering on the calculated values are related to flux variations during sampling process.

The spectral response of the photoanodes was determined by Incident Photon to Current Efficiency (IPCE) measurements (**Figure 1d**). Pristine $BiVO_4$ exhibits a photocurrent onset around 525 nm, in good agreement with previous studies,[33] indicating that wavelengths above 550 nm are not contributing to photogeneration of carriers. A slight shift of the photocurrent onset to higher wavelengths can be observed for the reduced sample with a clear increase in the IPCE (%) for $\lambda <$ 550 nm, showing an improvement in the optical properties after the laser treatment. The estimated photocurrents from the IPCE measurements are 0.56 $mA \cdot cm^{-2}$ and 0.77 $mA \cdot cm^{-2}$ for the pristine and reduced $BiVO_4$, respectively, while those obtained from the LSV are 0.38 $mA \cdot cm^{-2}$ and 0.72 $mA \cdot cm^{-2}$, respectively. Additionally, the bandgap for both samples was extracted from the Tauc plot (Figure S6, Supporting Information), giving similar values of 2.43 eV and 2.45 eV for the reduced and pristine samples, respectively.

To unravel the origin of the enhanced behavior of the reduced samples, a combination of several material characterization techniques was employed along this study. Regarding the morphology, **Figures 2a** and **2b** show the SEM images of pristine and reduced sample, respectively. The pristine sample shows a granular surface with spherical grains sizing around 200 nm, while the reduced sample shows an interconnected dendritically planar surface with domains in the orders of microns (see also Figure S7, Supporting Information). The combination of a dense surface and larger domains could benefit the lifetime of the photogenerated holes, as previously reported for $BiVO_4$.[34] On the other hand, the cross-section images from secondary and back-scattered electrons (Figure S8, Supporting Information) depict the three components of the studied photoanodes (glass, FTO contact and $BiVO_4$ active layer) which can be clearly distinguished. The thickness of the FTO

layer is 300 nm while the $BiVO_4$ layers shows a thickness close to 500 nm. The increase in the grain size due to the laser treatment can be also observed.

Energy Dispersive X-Ray Spectroscopy (EDX) measurements (Figure S9 and S10, Supporting Information) confirm the presence, in stoichiometric proportion (Table S1, Supporting Information), of the expected elements from the active layer (Bi, V, O), the substrate (Si and Sn), as well as adventitious carbon, (C). No other elements were detected by this technique. The crystalline structure of the analyzed thin films samples was confirmed by X-Ray Diffraction (XRD), as shown in Figure 2c. All the indexed peaks for both samples correspond to the active monoclinic phase of $BiVO_4$ (Figure S11, Supporting Information), apart from the peaks at 26.5, 33.7 and 37.7º corresponding to the FTO substrates. In both cases, the presence of other compounds or phase segregations can be ruled out. Pawley analysis, shows an expansion in lattice parameters in the reduced sample (a=5,260782 Å, b=5,199361 Å and c=11,680757 Å), attributed to the presence of oxygen vacancies, compare with the pristine ones (a= 5,220597 Å, b= 5,118929 Å and c= 11,669325 Å).

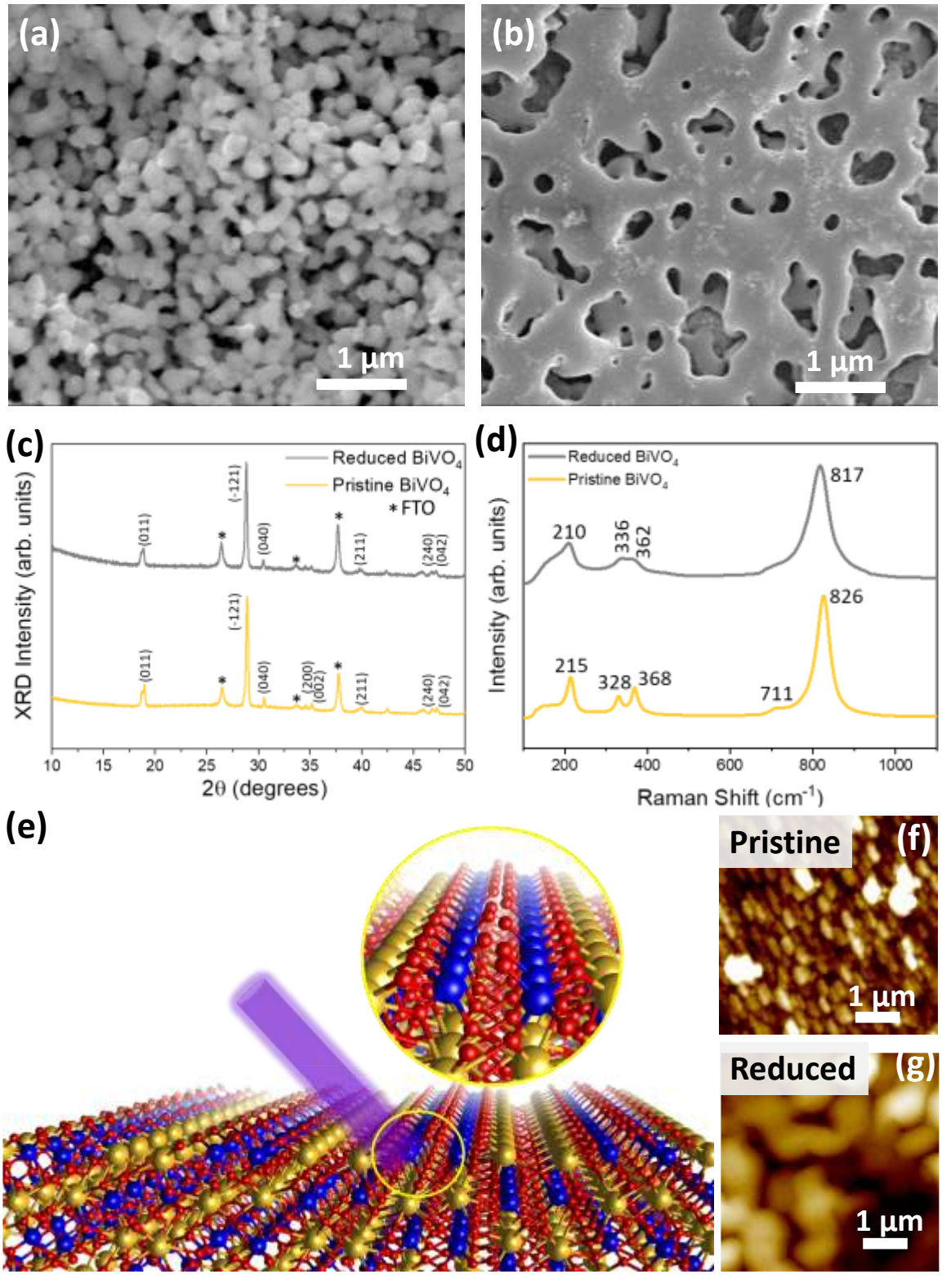
(a)
1 µm
(b)
1 µm
(c)
Reduced BiVO4
Pristine BiVO4
*FTO
XRD Intensity (arb. units)
2θ (degrees)
(d)
Reduced BiVO4
Pristine BiVO4
Intensity (arb. units)
Raman Shift (cm-1)
817
826
210
336
362
215
328
368
711
(e)
Pristine
(f)
1 µm
Reduced
(g)
1 µm

Figure 2. SEM images of the (a) pristine and (b) reduced sample. (c) XRD patterns of the analyzed samples. (d) Raman spectra of the analyzed samples. (e) (001) Surface of monoclinic $BiVO_4$ simulated with *VESTA* software (Bi in yellow, V in blue and O in red). AFM images of the (f) pristine and (g) reduced surface.

Additionally, the characteristic Raman vibrational modes associated with monoclinic $BiVO_4$ were clearly observed in the pristine sample, with peaks located at 215, 328, 368, 711 and 826 cm^{-1} (**Figure 2d**).[35,36] However, in the reduced sample, the detected peaks broadened and merged, and a red-shift was observed in all of them, as detailed in Figure S12, Supporting Information. This broadening has been associated with the formation of surface defects as oxygen vacancies,[18,37] while the red-shift could be attributed to the lattice expansion induced by the elongation of the V-O bonds as a consequence of the oxygen removal and the bigger ionic radii of V^{4+} compare with V^{5+},[38] in good agreement with XRD measurements. **Figure 2e** shows a representation of the (001) surface, which has been reported to be the most active for water oxidation, of monoclinic $BiVO_4$, while the inset shows the surface including some oxygen vacancies after the laser treatment. The morphology of the surface was also analyzed by Atomic Force Microscopy (**Figures 2f** and **2g**), where a saw-like relief formed by smaller grains can be observed in the pristine sample, while a less pronounced relief formed by more extended grains can be observed in the reduced sample, in good agreement with the SEM results. This is also confirmed by AFM 3D images (Figure S13, Supporting Information) where the surface relief is detailed.

Aiming to characterize the chemical state and the surface chemistry of the analyzed samples, both X-Ray Absorption (XAS) and X-Ray Photoelectron (XPS) spectroscopies were used. **Figure 3** displays the ultrahigh-vacuum Al Kα photoemission spectrum in the V 2p-O 1s, Bi 4f and valence band regions of the $BiVO_4$ thin films, before and after the laser irradiation treatment. The

spectrum of the as-prepared sample features intense peaks in the Bi 4f and V 2p regions with maxima at 158.7 and 516.5 eV, values which are well within the expected binding energy range for Bi(III) and V(V) cations, respectively.[39,40] The laser treatment brings about two significant changes to the spectrum: (i) a low binding energy component in V 2p region emerges, and (ii) a shift of the whole spectrum (core lines and VB) towards higher binding energy by about 0.38 eV, which can be clearly seen in the Bi 4f and VB regions. This indicates that a significant photoreduction process occurs in $BiVO_4$ upon laser irradiation. We can also observe that such reduction occurs selectively on V cations since the profile of the Bi 4f peak remains unchanged. Also, the contribution associated to reduced V species is about 1.2 eV below the main V 2p peak, at around 517 eV, which can be assigned to V(IV) cations.[41] Additionally, the surface reduction after the laser treatment was observed in the decrease in the ratio between lattice oxygen and vanadium extracted from the XPS analysis, as shown in Figure 3b and 3e. Reduced V species introduce electronic states above the VB, well within the band gap of $BiVO_4$, as clearly observed as a shoulder above the VB region of the photoelectron emission spectrum of the laser-treated sample (**Figure 3f**). These in-gap states can act as e^- density donor states, leading to an effective n-type doping of the system that pins the Fermi level to the conduction band.[42] Since all spectra are referenced to the Fermi level, this results in the observed shift of the spectrum of the laser-treated sample to higher BE. This shift represents a thermodynamically more favorable position of the energy bands to the water oxidation potential and hence an increased driving force towards this reaction.

Additionally, we evaluated the stability of V(IV) species under relevant H_2O environment by following the evolution of the photoelectron spectrum in the V 2p-O 1s region of the laser-treated sample, as the sample was exposed to increase pressures of H_2O vapour from Ultra High Vacuum

(UHV) to 1 mbar (Figure S14, Supporting Information) in a near-ambient pressure (NAP) XPS experiment.[43] Besides the increasing contribution of absorbed water species in the O 1s region around 535 eV, no significant changes were observed in the V 2p region. This observation suggests that generated V(IV) states and the associated electronic modulations are likely to be stable in the photoelectrodes during the PEC reaction.

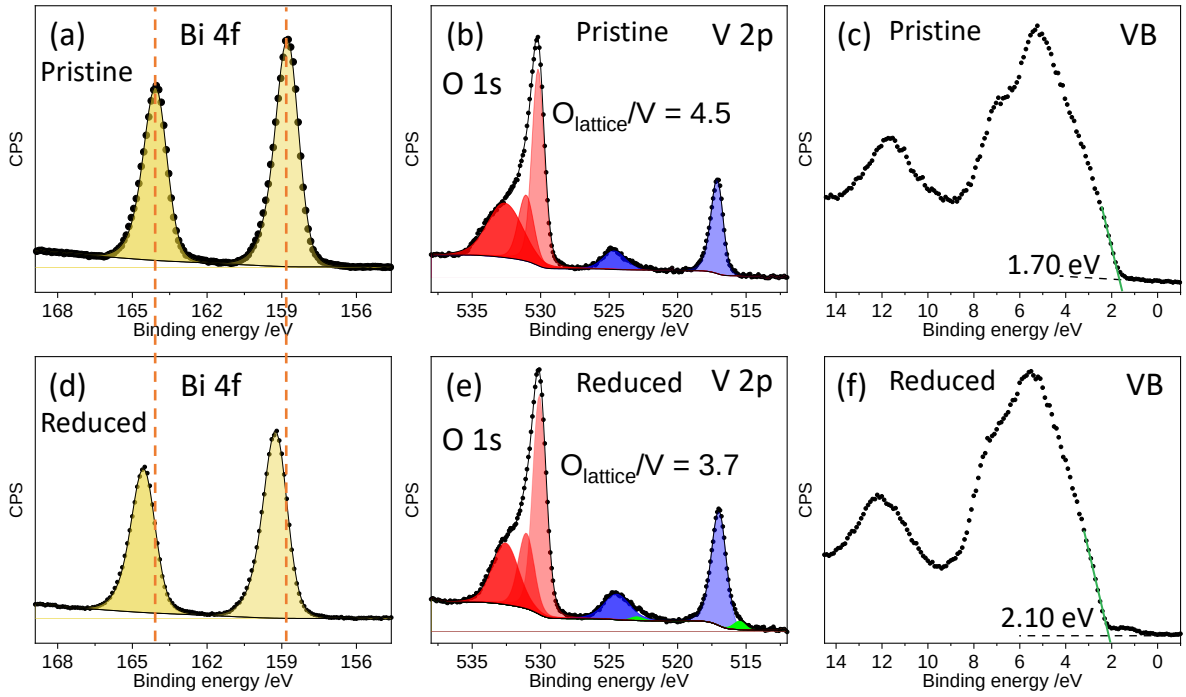

Figure 3. XPS measurements corresponding to the Bi 4f edge, V 2p-O 1s and valence band, acquired on the pristine (a, b and c) and reduced (d, e and f) $BiVO_4$ samples, respectively**.**

Once the surface reduction was confirmed by means of XPS, synchrotron-XAS measurements were performed to analyze if the reduction penetrates deeper in the bulk of the $BiVO_4$ films. Figure 4a shows the X-ray absorption near edge structure (XANES) of thin film samples and references. For comparison, a $BiVO_4$ film was calcinated under highly reducing H_2 atmosphere during 2h at 450 ºC in order to ensure a complete reduction of the film. The pristine and the laser-reduced

sample show practically identical spectral features. The samples show an intense pre-edge peak at 5469 eV that is associated to 1s-3d transitions. p-d transitions are electric-dipole forbidden but become allowed when there is a certain p-d orbital mixing, as it happens for tetrahedral coordination.[44] Spectral resonances at 5483 and 5502 eV are also in agreement with those reported by other authors for $BiVO_4$.[8] The edge position, around 5480 eV is similar to that of V_2O_5, indicating the presence of V^{5+} ions in the reduce film and the absence of detectable reduced vanadium species. Instead, there are remarkable spectral changes after exposure to H_2. The spectrum shifts towards lower energy and the edge is around 5477 eV. Two new resonances appear at around 5488 and 5500 eV, similar to V_2O_3.[45] The pre-edge peak decreases in intensity and this is a further confirmation of the reduction process occurred in the bulk of the sample. Moreover, a different local symmetry was obtained for the pristine and laser irradiated samples compared to the H_2-reduced film, as confirmed by the analysis of extended X-ray absorption fine structure (EXAFS).

The analysis of EXAFS spectra was performed in order to obtain more information about the local structure around vanadium ions before and after laser heating as well as after exposure to H_2.

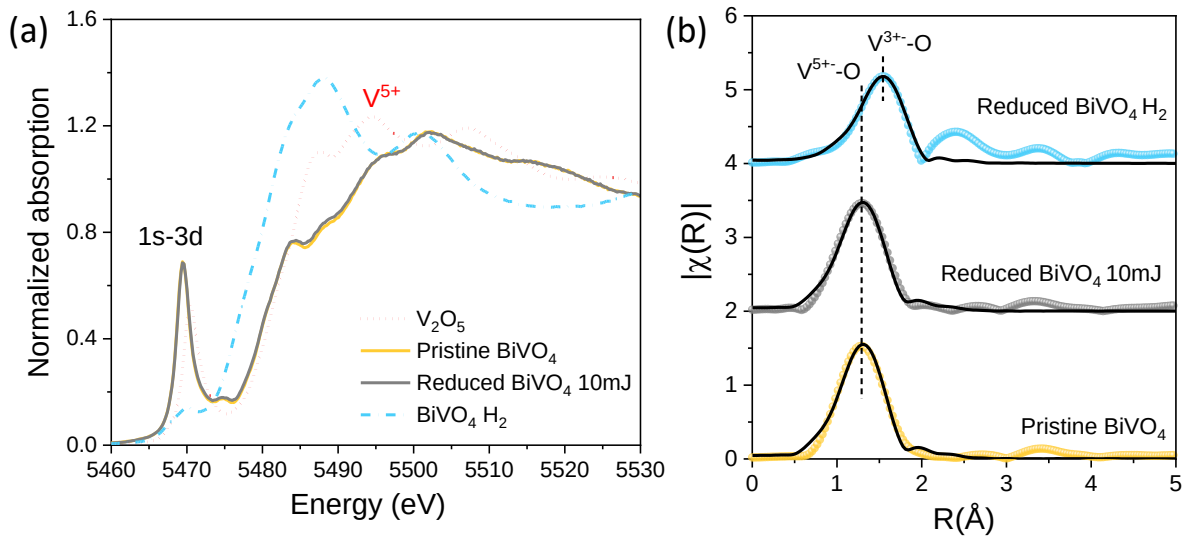

Figure 4. (a) Normalized XANES spectra at V K-edge of samples and V_2O_5 reference. (b) Fourier-transform moduli of the V K-edge EXAFS of data (sphere) and fit (black line) in the phase-shift-uncorrected scale.

The signal was analyzed in the k-range 3-11 Å and the fit performed using multiple k-weights, see **Figure 4b**. $BiVO_4$ can crystallize in orthorhombic, tetragonal and monoclinic phase, the monoclinic one being the only thermodynamically stable phase.[46,8] This structure has V^{5+} ions in tetrahedral coordination with O ions. For the pristine and laser reduced films the V-O coordination number was fixed to four and the average bond distance is 1.74 Å, in agreement with the average bond distance obtained from crystallographic data of the monoclinic structure,[46] see Table S2, Supporting Information. No relevant differences are observed in the EXAFS spectra of the samples after laser treatment, confirming the XANES results and the absence of bulk effects introduced upon laser irradiation. On the other side, for the film exposed to H_2, the coordination number of V-O shell was consistent with an octahedral geometry. Moreover, the reduction of vanadium was also confirmed by the relevant increase of the V-O bond distance to 2.01 Å, similar to the value reported for V_2O_3 species.[47] These results confirm the similarity of XAS and EXAFS spectra upon

laser irradiation, indicating that the changes occur only on the surface, as shown in the XPS results. In fact, XAS is an element selective technique sensitive to the average bulk properties and superficial changes are averaged out. Instead, only relevant changes are produced when the film were exposed to H_2 where the reduction process affects the whole bulk structure.

To investigate the role of the reduced species in the photoelectrochemical mechanism, Electrochemical Impedance Spectroscopy (EIS) and Transient Absorption Spectroscopy (TAS) were carried out. EIS measurements were performed in the dark and under illumination for the whole analyzed electrochemical window. Nyquist plots (Figure S15, Supporting Information) of the analyzed samples showed two arcs, and a consistent equivalent circuit previously employed for porous $BiVO_4$ photoanodes was employed for fitting the data.[48,49]

More specifically, due to the porous nature of the fabricated samples herein (by electrodeposition we achieve porous films, in contrast to other reported dense films of $BiVO_4$ deposited by spin-coated, for example)[50] we consider that the FTO substrate (C_{FTO}) is in contact with the electrolyte. The equivalent circuit (inset **Figure 5b**) also accounts for the charge transport (R_t) and charge transfer to the solution (R_{ct}), which are distributed and coupled along the electrode thickness, while R_s is the series resistance accounting for the contact and wiring.[51] The series resistance is within the 10-30 Ω cm^2 range for all the analyzed samples (Figure S16a, Supporting Information). However, the laser treatment induces a decrease in the charge transfer resistance (R_{ct}), **Figure 5a**, both in the dark and under illumination. Additionally, both the pristine and the reduced sample show a decrease in the R_{ct} with the anodic applied potential and with the illumination, as expected from an increase in the charge extraction due to a higher band bending. On the other hand, the extracted capacitances (**Figure 5b**) show the already reported feature with the applied potential for $BiVO_4$ photoanodes showing a peak at around 0.8 V vs RHE associated with V^{4+}/V^{5+} redox

transformation.[8,52] More interestingly, the reduced sample showed a clear decrease in the capacitance due an enhanced extraction as a consequence of a lower accumulation of carriers at the $BiVO_4$/electrolyte interface, especially at larger anodic bias, as well as a sharper peak at 0.8V vs RHE (Figure S16b, Supporting Information) which can be directly related with a higher amount of reduced V^{4+} states previous to the photoelectrochemistry, in good agreement with XPS measurements. The flatband position of the analyzed samples was extracted from Mott-Schottky analysis (Figure S17, Supporting Information), giving values of 0.05 and 0.1 V vs RHE for the pristine and reduced samples, respectively. These measurements, together with the Tauc analysis and the XPS measurements, allow the estimation of the band-energy positions (Figure S18, Supporting Information). A more favorable position of the valence band maximum (VBM) towards the water oxidation potential was confirmed for the reduced sample. The extracted capacitance from the FTO/electrolyte interface (Figure S19) shows a flat behavior with the applied potential, showing a constant value typical of a double layer capacitance, in good agreement with previous studies.[53]

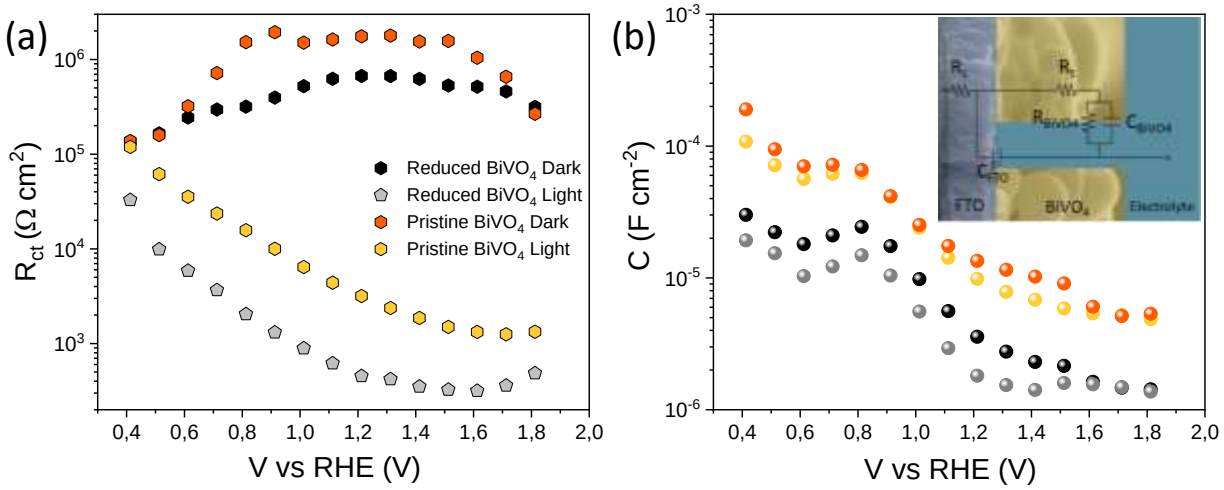

Figure 5. Extracted (a) charge transfer resistance, R_{ct}, and (b) capacitance, C, from the fitting of the EIS measurements. Inset showing the employed equivalent circuit superimposed on a cross-section SEM image accounting for the analyzed interfaces.

To further understand the role of the reduced $BiVO_4$ species and its implication on the charge dynamics, photoluminescence (PL) and transient absorption spectroscopy (TAS) experiments were performed.[54,55] Photoluminescence of pristine $BiVO_4$ resulted in an intense band centered at 430 nm exhibiting a bi-exponential lifetime (τ_F) of 11.2 and 69 ns (**Figure 6a and inset**). On the other hand, the radiative signal detected by PL has a maximum around 440 nm, which correspond to an energy of 2.8 eV. However, the bandgap of $BiVO_4$ is 2.4 eV, meaning that the observed optical signal corresponds to an above-edge emission (ABE). This phenomenon could be explained by the Moss-Burstein effect, consisting in the increasement of the apparent bandgap of a semiconductor as a result of some populated states close to the conduction band. This effect has been already reported in $BiVO_4$ due to the generation of electrons due to the presence of oxygen vacancies.[56,24] Additionally, the increase of laser pulses over the sample, lead to a decrease in the fluorescence emission of $BiVO_4$ as a consequence of the progressive reduction of the material (**Figure 6b**). This behavior was already observed on black TiO_2 mesocrystals containing oxygen vacancies, since the presence of these defects decrease the radiative recombination between free electrons and trapped holes, enhancing the catalytic activity.[57]

Firstly, the transient absorption spectrum of deaerated thin-film based on $BiVO_4$ exhibited a negative band in the range of 400-500 nm attributable to photoluminescence and a positive band from 500 nm corresponding to the photogenerated holes as it has been reported in the literature (**Figure 6c**, orange trace).[54,55] After fluorescence subtraction, this positive transient signal covers all the spectral window from 400 nm (**Figure 6c**, yellow trace). For reduced $BiVO_4$, a great

increase of the transient signal was observed from 450 nm, being at its maximum at around 600 nm (**Figure 6c**, grey trace).

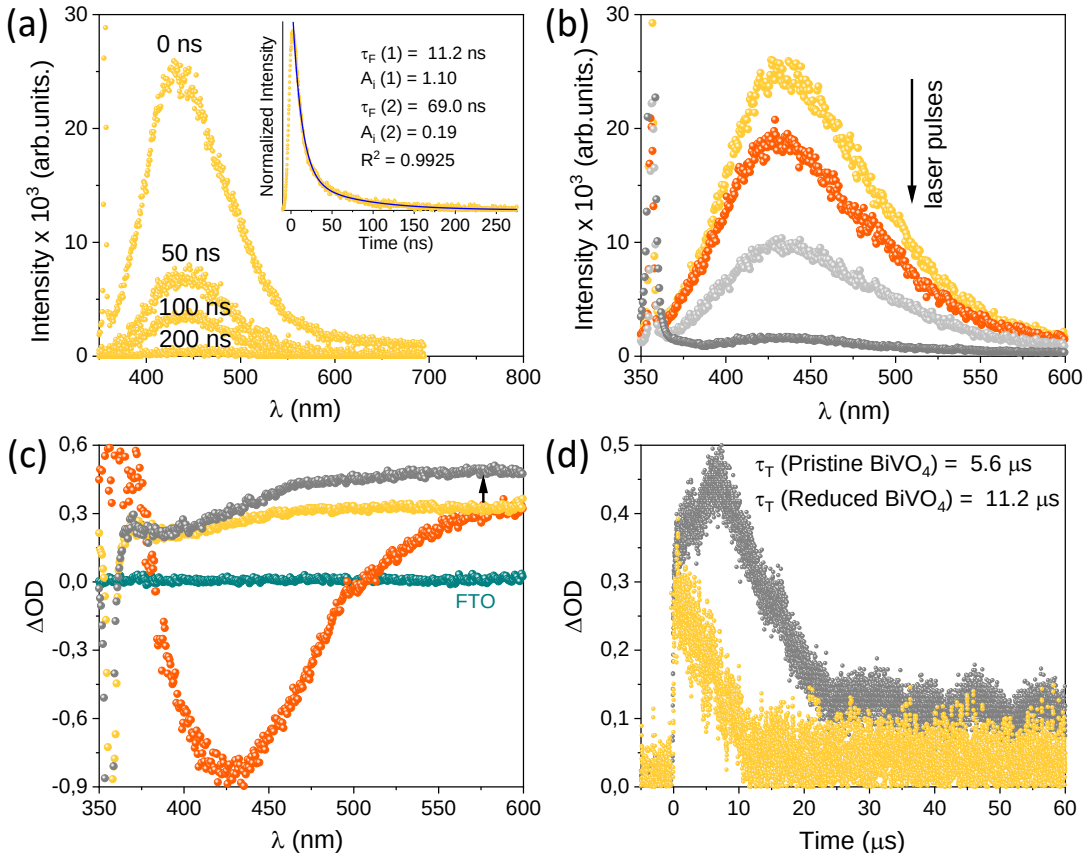

Figure 6. (a) Photoluminescence spectra (λ_{exc} = 355 nm) for $BiVO_4$ at different timescales. Inset: Decay trace (λ_{obs} = 430 nm). The fit is included (blue trace). (b) Photoluminescence spectra (λ_{exc} = 355 nm) for $BiVO_4$ upon increasing number of laser pulses. (c) Transient absorption spectra (TAS, λ_{exc} = 355 nm) for $BiVO_4$ (orange) immediately after the laser pulse and after fluorescence subtraction (yellow). TAS signal for reduced $BiVO_4$ (grey). FTO signal is included (turquoise). (d) Transient decay traces (λ_{exc} = 355 nm, λ_{obs} = 600 nm) for $BiVO_4$ (yellow) and reduced $BiVO_4$ (grey). All photophysical measurements were performed in deaerated thin films $BiVO_4$ over FTO immersed in 0.1 M KPi buffer.

More interestingly, a remarkable enhancement of the transient lifetime (τ_T), accompanied with a significant increase in signal intensity, was observed for the reduced $BiVO_4$ compared to the pristine $BiVO_4$ after monitoring at 600 nm, confirming a slow-down of the electron-hole pair recombination process (**Figure 6d**). Thus, while the temporal kinetic study for pristine $BiVO_4$ resulted in a transient lifetime of 5.6 μs (monitoring the first decay contribution), the reduced compound exhibited a long-lived τ_T of 11.2 μs in the same timescale range. Furthermore, the reduced $BiVO_4$ sample showed a large second contribution living above 60 μs timescale. This extended lifetime of the photogenerated holes could be attributed to the improved charge separation mediated by temporary carrier trapping at oxygen vacancies states in the reduced sample, as observed in other photoanodes.[58,59] On the other hand, the reduced lifetime in the pristine sample could be explained by an increase in the band to band recombination (free electrons in the conduction band recombine with valence band holes) due to the absence of oxygen vacancy states.[60]

The obtained results explain the greater performance as photoanodes of the reduced $BiVO_4$ compared to the pristine sample. The measured longer lifetime of photogenerated charges resulted from a slow non-coupled recombination in the microsecond scale, meaning that the photogenerated carriers can move further before recombining, in good agreement with the improved charge extraction observed by EIS based on the reduction of the capacitance, especially in the more anodic region**.**

Conclusions

The proposed laser irradiation method has been proved as a successfully surface reduction method to improve the performance of $BiVO_4$ towards water oxidation. Moreover, this method

selectively reduces superficial vanadium atoms and consequently creates oxygen vacancies without affecting the bulk of the films, as demonstrated by a combination of XPS and XAS. An effective n-doping was found in the reduced samples with a shift of the VBM to higher BE, leading to an enhance charge transport and a thermodynamically more favorable VB position towards water oxidation. Additionally, an extended lifetime of the photogenerated holes with a reduction in the charge transfer resistance and the accumulation of holes at the surface was found in the reduced sample, reducing recombination and boosting charge extraction, respectively. This phenomenon could be attributed to a combination of the changes in sample morphology and the optoelectronic properties, created after the sample treatment.

Experimental

Materials. Bismuth (III) nitrate ($Bi(NO_3)_3 \cdot 5H_2O \geq 98.0\%$), vanadyl acetylacetonate ($VO(acac)_2 \geq 97.0\%$), zirconyl chloride octahydrate ($ZrOCl_2 \cdot 8H_2O \geq 98.0\%$) and potassium phosphate monobasic and dibasic ($KH_2PO_4 \geq 99.0\%$ and $K_2HPO_4 \geq 98.0\%$). All reagents were acquired from sigma-Aldrich.

Synthesis of FTO-$BiVO_4$ electrodes. Zr doped $BiVO_4$ films were prepared following a previously reported method.[61] Metallic Bi was electrodeposited on glass substrates, coated with fluorine doped tin oxide (FTO), followed by a reaction with the vanadium precursor in DMSO, at 450 ºC for 2h. Zr precursor was added as 2.5 mol.% to the bismuth solution, according to a previously reported optimization process.[62]

Modification of $BiVO_4$ electrodes with laser treatment. To fabricate the reduced photoelectrodes, the pristine $BiVO_4$ samples were irradiated in air with the third harmonic (355

nm) of a Nd:YAG laser from EKSPLA, using different laser energies (1, 10, 20 and 30 mJ) for 30 s. No additional treatment was required.

X-Ray Diffraction (XRD). The crystal structure of $BiVO_4$ was characterized by using a diffractometer Philips PW 3040/00 X'Pert MPD/MRD with Cu Kα radiation (λ= 1.54178 Å) at a scanning rate of 0.2^{o} s^{-1}.

Field Emission-Scanning Electron Microscopy (FE-SEM). The morphology of the analysed samples was studied with a Field Emission SEM JEOL JSM-7900F, using LED and BED-C detectors, operating with 15 kV and a work distance (WD) between 2-10 mm. The EDX spectra were acquired with a ULTIM Max 170 from Oxford Instruments, equipped with Aztec software.

Raman Spectroscopy. The analysis was performed with a Jasco NRS-5100 spectrometer using a laser of 532 nm of wavelength at 5.3 mW power.

Near Ambient Pressure X-Ray Photoelectron Spectroscopy (NAP-XPS) measurements were recorded on a lab-based spectrometer (SPECS GmbH, Berlin) using a monochromated AlKα1 source (hν = 1486.6 eV) operating at 50 W. The X-rays are microfocused to give 300 μm a spot size on the samples. The spectrometer analyser is a SPECS PHOIBOS 150 NAP, a 180° hemispherical energy analyser with 150 mm mean radius. The entrance to the analyser is a nozzle with a 300 μm diameter orifice. The total energy resolution of the measurements was about 0.50 eV. The binding energy (BE) was calibrated against the Au Fermi level. Spectra were recorded in UHV as well as under H_2O pressures of at 0.1 mbar, 0.5 mbar and 1 mbar.

X-ray Absorption Spectroscopy (XAS) spectra at V K-edge were measured at the CLAESS beamline of the ALBA synchrotron[63] using a Si(111) double crystal monochromator cooled with

liquid nitrogen. Harmonic rejection was achieved by a proper combination of angle and coating of vertically collimating and focusing mirrors. The beam size at the sample position was adjusted to be around 400 x 400 μm^2. The $BiVO_4$ samples were measured in fluorescence mode using a six channels silicon drift detector. V_2O_5 was used as reference material and proper amount of sample powder was mixed with cellulose, press into pellet and measured in transmission mode by detecting the incident and transmitted intensity by two ionization chambers. A V foil was used for energy calibration. Data analysis was performed by ATHENA and ARTEMIS software.[64] Self-absorption corrections for fluorescence detection were also checked, and were negligible due to the small thickness of the samples.

Atomic Force Microscopy (AFM) was performed with a XE-100 Park equipment.

Ultraviolet–Visible Diffuse Reflectance Spectra (UV–Vis DRS) were performed with a Perkin Elmer Lambda 1050 UV/Vis/NIR spectrometer. Tauc Plot equation ($\alpha h\nu^{\gamma} = A(h\nu - E_g)$, where the absorption coefficient (α) is related to the incident photon energy ($h\nu$), A is constant, γ is the index indicating the type of transition) were employed for the quantification of the band gap transition. was determined from the steep shape of the spectra and the equation.

Laser Flash Photolysis (LFP). Both Steady-State and Time-Resolved Photoluminescence as well as Transient Absorption Spectroscopy (TAS) measurements were carried out with a laser flash equipment from Edinburgh Instruments (LP980) based on an optical parametric oscillator (OPO) pumped by the third harmonic of a Nd:YAG laser (EKSPLA). For the emission measurements at 355 nm, the probe shutter is closed so that no light from the Xe lamp is exciting the sample and only the laser is used as a light source. It is thus possible to use the LP980 system to acquire spectral luminescence and decays. For the transient absorption experiments, the selected

excitation wavelength for the measurements was 355 nm with single low energy pulses of 500 μJ/pulse while a pulsed xenon flash lamp (150 W) of 5 ns duration was employed as detecting light source. The probe light is dispersed through a monochromator (TMS302-A, grating 150 lines/mm) after it has passed the sample and then reaches a PMT detector (Hamamatsu Photonics) to obtain the temporal profile. All transient spectra and kinetics were recorded at room temperature using 1 x 1 cm quartz cells introducing a thin-film sample into the cuvette. Aqueous potassium phosphate 0.1 M (pH = 7) was used as solvent, which were bubbled for 15 min with N_2 before acquisition.

Photoelectrochemical Characterisation. All photoelectrochemical experiments were performed under three-electrode configuration in an electrochemical cell with a quartz window containing an aqueous solution of 0.1 M KPi buffer pH=7.5. An Ag/AgCl electrode was employed as the reference, a Pt wire as the counter electrode and the fabricated photoelectrode as the working electrode. These experiments were performed with a potentiostat-galvanostat PGSTAT204 provided with an integrated impedance module FRAII. A solar simulator (LOT LSH302 Xe lamp and an LSZ389 AM1.5 global filter) calibrated as 1 Sun (100m W/cm^2) was used as a light source. Linear sweep voltammetry (LSV) measurements were performed at 20 mV s^{-1}, while cyclic voltammetries (CV) were carried out at 50 mV s^{-1}. The charge separation and catalytic efficiencies were calculated following the equations $j_{H_2O} = j_{abs} \cdot \eta_{cs} \cdot \eta_{cat}$ and $j_{HS} = j_{abs} \cdot \eta_{cs}$, where j_{H_2O} is the current density in the presence of KPi electrolyte (aqueous), j_{HS} is the current density in the presence of Na_2SO_3 1M as hole scavenger and j_{abs} is the theoretical maximum photocurrent. To calculate the Faradaic efficiency, the amount of generated O_2 was measured every 3.5 min during a chronoamperometric measurement at 1.23 V versus RHE in 0.1 M KPi buffer (pH=7.5), using an electrochemical glass-sealed cell coupled to a gas chromatograph.

Electrochemical Impedance Spectroscopy (EIS) experiments were performed along the whole potential window at a selected potential with a sinusoidal perturbation of 20 mV and a frequency range from 400 kHz to 100 mHz. All potentials were referred to RHE through the Nerst equation:

$$V_{RHE} = V^{0}_{Ag/AgCl} + V_{Ag/AgCl} + (0.059 \cdot pH)$$

ACKNOWLEDGMENTS

This work was supported by the national projects funded by MCIN/ AEI /10.13039/50110001103 Nhympha (PID2019-106315RB-I00), NovaCO2 (PID2020-118593RB-C22) and SOL-Future (PLEC2021-007906) funded also by the European Union NextGenerationEU/ PRTR. Author also would like to aknowledge the regional project FotoArt-CM (S2018/NMT-4367) funded by Comunidad de Madrid. M.B. thanks the Spanish MICINN the *Juan de la Cierva Incorporación* grant (IJC2019 – 042430 –I). XAS measurements were performed at the BL22-CLAESS beamline at the ALBA synchrotron with the collaboration of ALBA staff under the experiment number 2020094687. The researchers wish to thank Dr. Fernando Picó for his valuable help in acquiring FESEM and AFM images and the X-ray diffractograms.

Corresponding Authors:

Víctor A. de la Peña O´Shea. *Photoactivated Processes Unit, IMDEA Energy, Avda. Ramón de la Sagra, 3, Móstoles, 28935, Spain.* Email: victor.delapenya@imdea.org

Miguel García-Tecedor. *Photoactivated Processes Unit, IMDEA Energy, Avda. Ramón de la Sagra, 3, Móstoles, 28935, Spain.* Email: miguel.tecedor@imdea.org

Supporting Information. Complementary Photoelectrochemical characterization; Tauc Plot; Complementary SEM and EDX; Lattice structure; Detailed Raman; Detailed AFM; Near Ambient Pressure-X-Ray Photoelectron Spectroscopy (NAP-XPS); Complementary Electrochemical Impedance Spectroscopy.

REFERENCES

(1) Kudo, A.; Ueda, K.; Kato, H.; Mikami, I. Photocatalytic O_2 Evolution under Visible Light Irradiation on $BiVO_4$ in Aqueous $AgNO_3$ Solution. *Catal. Letters* **1998**, *53*, 229–230.

(2) Tokunaga, S.; Kato, H.; Kudo, A. Selective Preparation of Monoclinic and Tetragonal $BiVO_4$ with Scheelite Structure and Their Photocatalytic Properties. *Chem. Mater.* **2001**, *13* (12), 4624–4628. https://doi.org/10.1021/cm0103390.

(3) Abdi, F. F.; Van De Krol, R. Nature and Light Dependence of Bulk Recombination in Co-Pi-Catalyzed $BiVO_4$ Photoanodes. *J. Phys. Chem. C* **2012**, *116* (17), 9398–9404. https://doi.org/10.1021/jp3007552.

(4) Abdi, F. F.; Savenije, T. J.; May, M. M.; Dam, B.; Van De Krol, R. The Origin of Slow Carrier Transport in $BiVO_4$ Thin Film Photoanodes: A Time-Resolved Microwave Conductivity Study. *J. Phys. Chem. Lett.* **2013**, *4* (16), 2752–2757. https://doi.org/10.1021/jz4013257.

(5) Zachäus, C.; Abdi, F. F.; Peter, L. M.; Van De Krol, R. Photocurrent of $BiVO_4$ Is Limited by Surface Recombination, Not Surface Catalysis. *Chem. Sci.* **2017**, *8* (5), 3712–3719. https://doi.org/10.1039/c7sc00363c.

(6) Pihosh, Y.; Turkevych, I.; Mawatari, K.; Uemura, J.; Kazoe, Y.; Kosar, S.; Makita, K.; Sugaya, T.; Matsui, T.; Fujita, D.; Tosa, M.; Kondo, M.; Kitamori, T. Photocatalytic Generation of Hydrogen by Core-Shell $WO_3/BiVO_4$ Nanorods with Ultimate Water Splitting Efficiency. *Sci. Rep.* **2015**, *5* (February), 1–2. https://doi.org/10.1038/srep11141.

(7) Su, J.; Guo, L.; Bao, N.; Grimes, C. A. Nanostructured $WO_3/BiVO_4$ Heterojunction Films for Efficient Photoelectrochemical Water Splitting. *Nano Lett.* **2011**, *11* (5), 1928–1933. https://doi.org/10.1021/nl2000743.

(8) Trześniewski, B. J.; Digdaya, I. A.; Nagaki, T.; Ravishankar, S.; Herraiz-Cardona, I.; Vermaas, D. A.; Longo, A.; Gimenez, S.; Smith, W. A. Near-Complete Suppression of Surface Losses and Total Internal Quantum Efficiency in $BiVO_4$ Photoanodes. *Energy Environ. Sci.* **2017**, *10* (6), 1517–1529. https://doi.org/10.1039/c6ee03677e.

(9) Lamm, B.; Trześniewski, B. J.; Döscher, H.; Smith, W. A.; Stefik, M. Emerging Postsynthetic Improvements of $BiVO_4$ Photoanodes for Solar Water Splitting. *ACS Energy Lett.* **2018**, *3* (1), 112–124. https://doi.org/10.1021/acsenergylett.7b00834.

(10) Li, T.; He, J.; Peña, B.; Berlinguette, C. P. Curing $BiVO_4$ Photoanodes with Ultraviolet Light Enhances Photoelectrocatalysis. *Angew. Chemie - Int. Ed.* **2016**, *55* (5), 1769–1772. https://doi.org/10.1002/anie.201509567.

(11) Arcas, R.; Cardenas-Morcoso, D.; Spadaro, M. C.; García-Tecedor, M.; Mesa, C. A.; Arbiol, J.; Fabregat-Santiago, F.; Giménez, S.; Mas-Marzá, E. Direct Observation of the Chemical Transformations in BiVO 4 Photoanodes upon Prolonged Light-aging Treatments . *Sol. RRL* **2022**. https://doi.org/10.1002/solr.202200132.

(12) Cui, H.; Zhao, W.; Yang, C.; Yin, H.; Lin, T.; Shan, Y.; Xie, Y.; Gu, H.; Huang, F. Black TiO_2 Nanotube Arrays for High-Efficiency Photoelectrochemical Water-Splitting. *J. Mater. Chem. A* **2014**, *2* (23), 8612–8616. https://doi.org/10.1039/c4ta00176a.

(13) Pesci, F. M.; Wang, G.; Klug, D. R.; Li, Y.; Cowan, A. J. E Ffi Cient Suppression of Electron − Hole Recombination in Oxygen- De Fi Cient Hydrogen-Treated TiO 2 Nanowires for Photoelectrochemical Water Splitting. **2013**.

(14) Xiaobo Chen, Lei Liu, Peter Y. Yu, S. S. M. Increasing Solar Absorption for Photocatalysis with Black Hydrogenated Titanium Dioxide Nanocrystals. *Science (80-.).* **2011**, *331* (6018), 746–750.

(15) Corby, S.; Rao, R. R.; Steier, L.; Durrant, J. R. The Kinetics of Metal Oxide Photoanodes from Charge Generation to Catalysis. *Nat. Rev. Mater.* **2021**, *6* (12), 1136–1155. https://doi.org/10.1038/s41578-021-00343-7.

(16) Fernández-Climent, R.; Giménez, S.; García-Tecedor, M. The Role of Oxygen Vacancies in Water Splitting Photoanodes. *Sustain. Energy Fuels* **2020**, *4* (12), 5916–5926. https://doi.org/10.1039/d0se01305f.

(17) Wang, Z.; Wang, L. Role of Oxygen Vacancy in Metal Oxide Based Photoelectrochemical Water Splitting. *EcoMat* **2021**, *3* (1), 1–13. https://doi.org/10.1002/eom2.12075.

(18) Wang, G.; Ling, Y.; Lu, X.; Qian, F.; Tong, Y.; Zhang, J. Z.; Lordi, V.; Rocha Leao, C.; Li, Y. Computational and Photoelectrochemical Study of Hydrogenated Bismuth Vanadate. *J. Phys. Chem. C* **2013**, *117* (21), 10957–10964. https://doi.org/10.1021/jp401972h.

(19) Wang, S.; Chen, P.; Bai, Y.; Yun, J. H.; Liu, G.; Wang, L. New $BiVO_4$ Dual Photoanodes with Enriched Oxygen Vacancies for Efficient Solar-Driven Water Splitting. *Adv. Mater.* **2018**, *30* (20), 1–7. https://doi.org/10.1002/adma.201800486.

(20) Wang, S.; He, T.; Chen, P.; Du, A.; Ostrikov, K.; Huang, W.; Wang, L. In Situ Formation of Oxygen Vacancies Achieving Near-Complete Charge Separation in Planar $BiVO_4$ Photoanodes. *Adv. Mater.* **2020**, *32* (26), 1–10. https://doi.org/10.1002/adma.202001385.

(21) Tian, Z.; Zhang, P.; Qin, P.; Sun, D.; Zhang, S.; Guo, X.; Zhao, W.; Zhao, D.; Huang, F. Novel Black $BiVO_4/TiO_{2-x}$ Photoanode with Enhanced Photon Absorption and Charge Separation for Efficient and Stable Solar Water Splitting. *Adv. Energy Mater.* **2019**, *9* (27), 1–8. https://doi.org/10.1002/aenm.201901287.

(22) Feng, S.; Wang, T.; Liu, B.; Hu, C.; Li, L.; Zhao, Z.; Gong, J. Enriched Surface Oxygen Vacancies of Photoanodes by Photoetching with Enhanced Charge Separation. *Angew.*

Chemie **2020**, *132* (5), 2060–2064. https://doi.org/10.1002/ange.201913295.

(23) Peng, Y.; Wu, H.; Yuan, M.; Li, F. F.; Zou, X.; Ng, Y. H.; Hsu, H. Y. Chemical Reduction-Induced Surface Oxygen Vacancies of BiVO4photoanodes with Enhanced Photoelectrochemical Performance. *Sustain. Energy Fuels* **2021**, *5* (8), 2284–2293. https://doi.org/10.1039/d0se01901a.

(24) Selim, S.; Pastor, E.; García-Tecedor, M.; Morris, M. R.; Francàs, L.; Sachs, M.; Moss, B.; Corby, S.; Mesa, C. A.; Gimenez, S.; Kafizas, A.; Bakulin, A. A.; Durrant, J. R. Impact of Oxygen Vacancy Occupancy on Charge Carrier Dynamics in $BiVO_4$ Photoanodes. *J. Am. Chem. Soc.* **2019**, *141* (47), 18791–18798. https://doi.org/10.1021/jacs.9b09056.

(25) Jin, S.; Ma, X.; Pan, J.; Zhu, C.; Saji, S. E.; Hu, J.; Xu, X.; Sun, L.; Yin, Z. Oxygen Vacancies Activating Surface Reactivity to Favor Charge Separation and Transfer in Nanoporous $BiVO_4$ Photoanodes. *Appl. Catal. B Environ.* **2021**, *281* (July 2020), 119477. https://doi.org/10.1016/j.apcatb.2020.119477.

(26) Klahr, B.; Gimenez, S.; Fabregat-Santiago, F.; Bisquert, J.; Hamann, T. W. Electrochemical and Photoelectrochemical Investigation of Water Oxidation with Hematite Electrodes. *Energy Environ. Sci.* **2012**, *5* (6), 7626–7636. https://doi.org/10.1039/c2ee21414h.

(27) López-Calixto, C. G.; Barawi, M.; Gomez-Mendoza, M.; Oropeza, F. E.; Fresno, F.; Liras, M.; De La Penã O'Shea, V. A. Hybrids Based on BOPHY-Conjugated Porous Polymers as Photocatalysts for Hydrogen Production: Insight into the Charge Transfer Pathway. *ACS Catal.* **2020**, *10* (17). https://doi.org/10.1021/acscatal.0c01346.

(28) Barroso, M.; Pendlebury, S. R.; Cowan, A. J.; Durrant, J. R. Charge Carrier Trapping, Recombination and Transfer in Hematite (α-Fe_2O_3) Water Splitting Photoanodes. *Chem. Sci.* **2013**, *4* (7), 2724–2734. https://doi.org/10.1039/c3sc50496d.

(29) Ma, Y.; Le Formal, F.; Kafizas, A.; Pendlebury, S. R.; Durrant, J. R. Efficient Suppression of Back Electron/Hole Recombination in Cobalt Phosphate Surface-Modified Undoped Bismuth Vanadate Photoanodes. *J. Mater. Chem. A* **2015**, *3* (41), 20649–20657. https://doi.org/10.1039/c5ta05826k.

(30) Collado, L.; Naranjo, T.; Gomez-Mendoza, M.; López-Calixto, C. G.; Oropeza, F. E.; Liras, M.; Marugán, J.; de la Peña O'Shea, V. A. Conjugated Porous Polymers Based on BODIPY and BOPHY Dyes in Hybrid Heterojunctions for Artificial Photosynthesis. *Adv. Funct. Mater.* **2021**, *31* (51), 2105384. https://doi.org/https://doi.org/10.1002/adfm.202105384.

(31) Steier, L.; Herraiz-Cardona, I.; Gimenez, S.; Fabregat-Santiago, F.; Bisquert, J.; Tilley, S. D.; Grätzel, M. Understanding the Role of Underlayers and Overlayers in Thin Film Hematite Photoanodes. *Adv. Funct. Mater.* **2014**, *24* (48), 7681–7688. https://doi.org/10.1002/adfm.201402742.

(32) Liang, Y.; Tsubota, T.; Mooij, L. P. A.; Van De Krol, R. Highly Improved Quantum Efficiencies for Thin Film BiVO4 Photoanodes. *J. Phys. Chem. C* **2011**, *115* (35), 17594–17598. https://doi.org/10.1021/jp203004v.

(33) Shaddad, M. N.; Cardenas-Morcoso, D.; Arunachalam, P.; García-Tecedor, M.; Ghanem, M. A.; Bisquert, J.; Al-Mayouf, A.; Gimenez, S. Enhancing the Optical Absorption and Interfacial Properties of $BiVO_4$ with Ag_3PO_4 Nanoparticles for Efficient Water Splitting. *J. Phys. Chem. C* **2018**, *122* (22), 11608–11615. https://doi.org/10.1021/acs.jpcc.8b00738.

(34) Yabuta, M.; Takeda, A.; Sugimoto, T.; Watanabe, K.; Kudo, A.; Matsumoto, Y. Particle Size Dependence of Carrier Dynamics and Reactivity of Photocatalyst $BiVO_4$ Probed with Single-Particle Transient Absorption Microscopy. *J. Phys. Chem. C* **2017**, *121* (40), 22060–22066. https://doi.org/10.1021/acs.jpcc.7b06230.

(35) Wang, S.; Chen, P.; Yun, J.-H.; Hu, Y.; Wang, L. An Electrochemically Treated $BiVO_4$ Photoanode for Efficient Photoelectrochemical Water Splitting . *Angew. Chemie* **2017**, *129* (29), 8620–8624. https://doi.org/10.1002/ange.201703491.

(36) Frost, R. L.; Henry, D. A.; Weier, M. L.; Martens, W. Raman Spectroscopy of Three Polymorphs of $BiVO_4$: Clinobisvanite, Dreyerite and Pucherite, with Comparisons to (VO_4) 3-Bearing Minerals: Namibite, Pottsite and Schumacherite. *J. Raman Spectrosc.* **2006**, *37* (7), 722–732. https://doi.org/10.1002/jrs.1499.

(37) Österbacka, N.; Wiktor, J. Influence of Oxygen Vacancies on the Structure of $BiVO_4$. *J. Phys. Chem. C* **2021**, *125* (2), 1200–1207. https://doi.org/10.1021/acs.jpcc.0c08751.

(38) http://abulafia.mt.ic.ac.uk/shannon/ptable.php.

(39) Zhang, B.; Huang, X.; Zhang, Y.; Lu, G.; Chou, L.; Bi, Y. Unveiling the Activity and Stability Origin of BiVO4 Photoanodes with FeNi Oxyhydroxides for Oxygen Evolution. *Angew. Chemie - Int. Ed.* **2020**, *59* (43), 18990–18995. https://doi.org/10.1002/anie.202008198.

(40) Zhong, M.; Hisatomi, T.; Kuang, Y.; Zhao, J.; Liu, M.; Iwase, A.; Jia, Q.; Nishiyama, H.; Minegishi, T.; Nakabayashi, M.; Shibata, N.; Niishiro, R.; Katayama, C.; Shibano, H.; Katayama, M.; Kudo, A.; Yamada, T.; Domen, K. Surface Modification of CoO_x Loaded BiVO4 Photoanodes with Ultrathin P-Type NiO Layers for Improved Solar Water Oxidation. *J. Am. Chem. Soc.* **2015**, *137* (15), 5053–5060. https://doi.org/10.1021/jacs.5b00256.

(41) Silversmit, G.; Depla, D.; Poelman, H.; Marin, G. B.; De Gryse, R. Determination of the V2p XPS Binding Energies for Different Vanadium Oxidation States (V^{5+} to V^{0+}). *J. Electron Spectros. Relat. Phenomena* **2004**, *135* (2–3), 167–175.

https://doi.org/10.1016/j.elspec.2004.03.004.

(42) Qin, D. D.; Wang, T.; Song, Y. M.; Tao, C. L. Reduced Monoclinic $BiVO_4$ for Improved Photoelectrochemical Oxidation of Water under Visible Light. *Dalt. Trans.* **2014**, *43* (21), 7691–7694. https://doi.org/10.1039/c3dt53575d.

(43) Shen, Z.; Zhuang, Y.; Li, W.; Huang, X.; Oropeza, F. E.; Hensen, E. J. M.; Hofmann, J. P.; Cui, M.; Tadich, A.; Qi, D.; Cheng, J.; Li, J.; Zhang, K. H. L. Increased Activity in the Oxygen Evolution Reaction by Fe4+-Induced Hole States in Perovskite La1-: XSrxFeO3. *J. Mater. Chem. A* **2020**, *8* (8), 4407–4415. https://doi.org/10.1039/c9ta13313e.

(44) Markowicz, a; Wegrzynek, D.; Chinea-Cano, E.; Bamford, S. a; Torres, D. H.; Alvarez, R. P. Quality Management and Method Validation in EDXRF Analysis. *X-Ray Spectrom.* **2007**, *36* (1), 27–34. https://doi.org/10.1002/xrs.

(45) Zhu, K.; Wei, S.; Shou, H.; Shen, F.; Chen, S.; Zhang, P.; Wang, C.; Cao, Y.; Guo, X.; Luo, M.; Zhang, H.; Ye, B.; Wu, X.; He, L.; Song, L. Defect Engineering on V_2O_3 Cathode for Long-Cycling Aqueous Zinc Metal Batteries. *Nat. Commun.* **2021**, *12* (1), 1–9. https://doi.org/10.1038/s41467-021-27203-w.

(46) Ding, K.; Chen, B.; Li, Y.; Zhang, Y.; Chen, Z. Comparative Density Functional Theory Study on the Electronic and Optical Properties of BiMO4 (M = V, Nb, Ta). *J. Mater. Chem. A* **2014**, *2* (22), 8294–8303. https://doi.org/10.1039/c3ta15367c.

(47) Tenailleau, C.; Suard, E.; Rodriguez-Carvajal, J.; Gibaud, A.; Lacorre, P. Effect of Doping and Temperature on the Crystal Structure of $(V_{1-X}MO_x)_2O_3$ above and below the Metal/Insulator Transition. *J. Solid State Chem.* **2003**, *174* (2), 431–440. https://doi.org/10.1016/S0022-4596(03)00295-0.

(48) Han, L.; González-Cobos, J.; Sánchez-Molina, I.; Giancola, S.; Folkman, S. J.; Tang, P.;

Heggen, M.; Dunin-Borkowski, R. E.; Arbiol, J.; Giménez, S.; Galan-Mascaros, J. R. Cobalt Hexacyanoferrate as a Selective and High Current Density Formate Oxidation Electrocatalyst. *ACS Appl. Energy Mater.* **2020**, *3* (9), 9198–9207. https://doi.org/10.1021/acsaem.0c01548.

(49) Shi, X.; Herraiz-Cardona, I.; Bertoluzzi, L.; Lopez-Varo, P.; Bisquert, J.; Park, J. H.; Gimenez, S. Understanding the Synergistic Effect of WO_3-$BiVO_4$ Heterostructures by Impedance Spectroscopy. *Phys. Chem. Chem. Phys.* **2016**, *18* (13), 9255–9261. https://doi.org/10.1039/c5cp07905e.

(50) Selim, S.; Francàs, L.; García-Tecedor, M.; Corby, S.; Blackman, C.; Gimenez, S.; Durrant, J. R.; Kafizas, A. WO_3/$BiVO_4$: Impact of Charge Separation at the Timescale of Water Oxidation. *Chem. Sci.* **2019**, *10* (9). https://doi.org/10.1039/c8sc04679d.

(51) Klahr, B.; Gimenez, S.; Fabregat-Santiago, F.; Bisquert, J.; Hamann, T. W. Photoelectrochemical and Impedance Spectroscopic Investigation of Water Oxidation with "Co-Pi"-Coated Hematite Electrodes. *J. Am. Chem. Soc.* **2012**, *134* (40), 16693–16700. https://doi.org/10.1021/ja306427f.

(52) Cardenas-Morcoso, D.; Ifraemov, R.; García-Tecedor, M.; Liberman, I.; Gimenez, S.; Hod, I. A Metal-Organic Framework Converted Catalyst That Boosts Photo-Electrochemical Water Splitting. *J. Mater. Chem. A* **2019**, *7* (18). https://doi.org/10.1039/c9ta01559k.

(53) Fabregat-Santiago, F.; Garcia-Belmonte, G.; Bisquert, J.; Bogdanoff, P.; Zaban, A. Mott-Schottky Analysis of Nanoporous Semiconductor Electrodes in Dielectric State Deposited on SnO_2(F) Conducting Substrates. *J. Electrochem. Soc.* **2003**, *150* (6), E293. https://doi.org/10.1149/1.1568741.

(54) Ma, Y.; Pendlebury, S. R.; Reynal, A.; Le Formal, F.; Durrant, J. R. Dynamics of

Photogenerated Holes in Undoped $BiVO_4$ Photoanodes for Solar Water Oxidation. *Chem. Sci.* **2014**, *5* (8), 2964–2973. https://doi.org/10.1039/c4sc00469h.

(55) Ravensbergen, J.; Abdi, F. F.; Van Santen, J. H.; Frese, R. N.; Dam, B.; Van De Krol, R.; Kennis, J. T. M. Unraveling the Carrier Dynamics of $BiVO_4$: A Femtosecond to Microsecond Transient Absorption Study. *J. Phys. Chem. C* **2014**, *118* (48), 27793–27800. https://doi.org/10.1021/jp509930s.

(56) Maheskumar, V.; Jiang, Z.; Lin, Y.; Vidhya, B.; Sasikumar, S. Synergistic Effect of Ag and Cu Co-Doping on the Structural, Optical, and Photocatalytic Performance of $BiVO_4$. *J. Mater. Sci. Mater. Electron.* **2021**, *32* (19), 23811–23824. https://doi.org/10.1007/s10854-021-06717-5.

(57) Elbanna, O.; Fujitsuka, M.; Kim, S.; Majima, T. Charge Carrier Dynamics in TiO_2 Mesocrystals with Oxygen Vacancies for Photocatalytic Hydrogen Generation under Solar Light Irradiation. *J. Phys. Chem. C* **2018**, *122* (27), 15163–15170. https://doi.org/10.1021/acs.jpcc.8b04026.

(58) Yu, H.; Li, J.; Zhang, Y.; Yang, S.; Han, K.; Dong, F.; Ma, T.; Huang, H. Three-in-One Oxygen Vacancies: Whole Visible-Spectrum Absorption, Efficient Charge Separation, and Surface Site Activation for Robust CO_2 Photoreduction. *Angew. Chemie - Int. Ed.* **2019**, *58* (12), 3880–3884. https://doi.org/10.1002/anie.201813967.

(59) Ansari, S. A.; Khan, M. M.; Kalathil, S.; Nisar, A.; Lee, J.; Cho, M. H. Oxygen Vacancy Induced Band Gap Narrowing of ZnO Nanostructures by an Electrochemically Active Biofilm. *Nanoscale* **2013**, *5* (19), 9238–9246. https://doi.org/10.1039/c3nr02678g.

(60) Corby, S.; Francàs, L.; Kafizas, A.; Durrant, J. R. Determining the Role of Oxygen Vacancies in the Photoelectrocatalytic Performance of WO_3 for Water Oxidation. *Chem.*

Sci. **2020**, *11* (11), 2907–2914. https://doi.org/10.1039/c9sc06325k.

(61) Kang, D.; Park, Y.; Hill, J. C.; Choi, K. Donghyeon Kang, Yiseul Park, James C. Hill, and Kyoung-Shin Choi. *J. Phys. Chem. Lett.* **2014**, *5*, 2994–2999.

(62) Kim, T. W.; Choi, K. S. Nanoporous $BiVO_4$ Photoanodes with Dual-Layer Oxygen Evolution Catalysts for Solar Water Splitting. *Science (80-.).* **2014**, *343* (6174), 990–994. https://doi.org/10.1126/science.1246913.

(63) Simonelli, L.; Marini, C.; Olszewski, W.; Ávila Pérez, M.; Ramanan, N.; Guilera, G.; Cuartero, V.; Klementiev, K. CLÆSS: The Hard X-Ray Absorption Beamline of the ALBA CELLS Synchrotron. *Cogent Phys.* **2016**, *3* (1), 1–10. https://doi.org/10.1080/23311940.2016.1231987.

(64) Ravel, B.; Newville, M. ATHENA, ARTEMIS, HEPHAESTUS: Data Analysis for X-Ray Absorption Spectroscopy Using IFEFFIT. *J. Synchrotron Radiat.* **2005**, *12* (4), 537–541. https://doi.org/10.1107/S0909049505012719.